ELSEVIER

Reciprocating excitation of a flexible beam: Benchmark study

R.G. Langlois, M.J.D. Hayes *

*Department of Mechanical and Aerospace Engineering, Carleton University, 3135 Mackenzie Building,
1125 Colonel By Drive, Ottawa, Ont., Canada K1S 5B6*

Abstract

A long and slender flexible beam is set in oscillatory motion to observe its deflection. A novel application of digital image processing is employed to obtain contactless discrete measurements of the beam tip deflection. We compare the measured data to those predicted by a flexible multibody dynamics simulation (FLXDYN). This study is intended as a benchmark. Moreover, the system is described in sufficient detail to enable other investigators to repeat, and build upon results herein presented for the first time.
© 2005 Elsevier Ltd. All rights reserved.

1. Introduction

Flexibility is an inherent property of structural members. It becomes one of major concern when mechanical systems are designed with tight shape and dimension tolerances, required to be lighter in weight, and to move at higher speeds. In addition there are many applications that use deformations, and corresponding strengths of structural members, to assemble machine components and avoid interference among parts: selectively compliant assembly robot arms (SCARA), for example. The dynamic characteristics of flexible beams, such as deflection under

---

* Corresponding author.
  E-mail addresses: rlangloi@mae.carleton.ca (R.G. Langlois), jhayes@mae.carleton.ca (M.J.D. Hayes).

inertial loading, are closely related to their material properties, geometry, and boundary conditions. Hence, a mathematical model and measurement system are required to experimentally determine characteristics of interest.

Multibody dynamics formulations have been proposed and refined since the 1970s that, using various levels of sophistication, include modelling of flexible bodies—both for systems having open- and closed-loop topology. Correspondingly, benchmark problems have been developed where alternative dynamics formulations have been compared with each other, and in some cases, to experimental results. Arguably, the two most common benchmark problems are the flexible beam spin-up problem for open-loop systems (see, for example, Haering et al. [1]) and the slider-crank mechanism for closed-loop systems (see, for example, Meijaard [2]). Many other benchmark problems have also been used. However, it is widely recognized that additional benchmark problems, that include aspects not present in published examples, would be of potentially lasting benefit to the multibody dynamics community. Further, development of measurement approaches that facilitate the collection of kinematic response data for flexible links in multibody systems could contribute to improving the availability of a greater number of published benchmark problems in the long term.

In this paper, we introduce a benchmark study in multibody dynamics via the examination of a flexible body undergoing reciprocating motion driven by a relatively stiff crank-rocker mechanism. We investigate the dynamic performance of flexible bodies using dynamic simulation, and empirical data for verification. The experimental apparatus, illustrated in Fig. 1, uses a commercially available long and slender aluminum beam as the flexible body. A motor-driven four-bar crank-rocker linkage provides reciprocating oscillations to excite the beam. The flexible beam is rigidly clamped to the relatively stiff rocker. The excitation angular frequency is measured using a rotational potentiometer. Surface strains are continuously measured at four locations along the length of the beam to estimate the coefficients of proportional damping. An *off-the-shelf* digital camera is used to acquire still images of the beam in motion. The rocker angle and beam deflection are extracted from the images thereby providing contactless measurements.
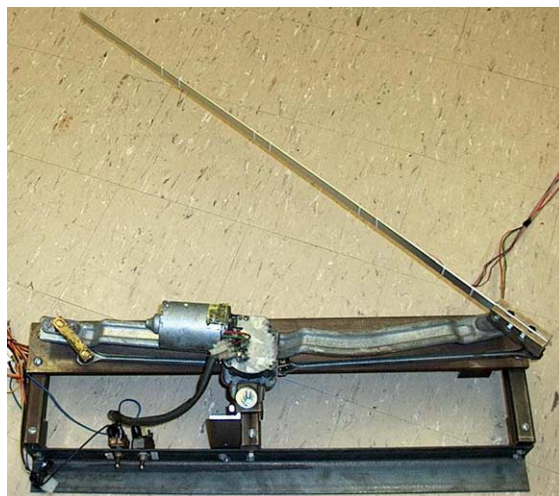

Fig. 1. Experimental apparatus.

The determination of the deflection of the beam and the angular position of the clamp using a contactless digital image processing approach is novel, up to the knowledge of the authors. Typically, such deflections are inferred from measurements obtained with surface-mounted strain gauges. The radial distortion of the lens is moderate, given the large field of view required for the 835 mm effective length of the clamped-free beam. However the linear distortion is eliminated by post-processing using principles of elementary projective geometry.

An analytical flexible multibody dynamics formulation is presented which automatically generates and solves the governing equation of the reciprocating beam problem. The code is an adapted version of FLXDYN [3]. The formulation does not place limits on the flexible bodies in terms of the magnitude of deformation or the level of internal damping. The code generates the time history of the moving beam starting from rest, through spin-up, to steady-state reciprocating motion. The output of the simulation is in agreement with the deflection of selected points along the length of the beam measured with the digital camera.

2. Experiment design and apparatus

Given the absence of literature examining open-loop flexible beam dynamics excited by reciprocating motion, we developed a reproducible benchmark study. The intention is to validate simulation results yielding lateral deflection of the beam under oscillating motion. The experimental apparatus consists of a long slender aluminum beam cantilevered to the rocker link of a planar crank-rocker mechanism such that the beam was flexible in a plane parallel to the plane of the mechanism, perpendicular to the gravity vector thereby mitigating its effects. The crank is driven by a geared-down DC motor. The beam dimensions are listed in Table 1.

Four $120 \pm 0.3 \ \Omega$ strain gauges are located at distances [5, 204, 403, 603] mm along the beam measured from the clamped end mounted to the rocker. The four strain gauges were bonded to the beam so their direction of sensitivity aligned with the longitudinal axis of the beam. A potentiometer is attached to the base-fixed revolute joint so as to measure its angular frequency. The effective length of the flexible beam is 835 mm. The mechanism configuration and strain gauge locations are shown pictorially and schematically in Figs. 1 and 2.

Static beam deflections were first measured and compared to static output from the simulation. For this purpose, the beam was removed from the crank-rocker mechanism and setup such that it would bend in a vertical plane as the result of weights associated with masses of different size suspended from the free end of the beam. The corresponding strains and tip displacements were measured under the effect of the applied loads. For each of three masses used, repeated readings of a precision ruled straight-edge were used to directly measure the difference between the vertical position of the beam tip prior to application of the tip weights and the deflected positions once the weights were attached and the system was allowed to settle to equilibrium.

Table 1
Flexible beam geometric parameters

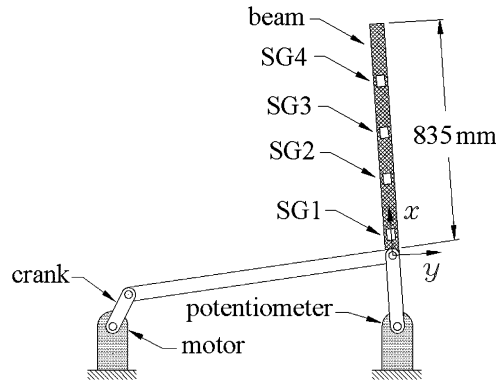| Height, h	Thickness, t	Clamp-free end length, l_c	Pivot point-free end length, l_p	Area moment of inertia, I_A
19.050 mm	3.175 mm	835.000 mm	843.000 mm	$5.08095 \times 10^{-11} \ \mathrm{m}^4$

Fig. 2. Schematic illustration of mechanism configuration and strain gauge attachment points.

For the dynamic testing the beam was mounted to the follower link using a rigid hub. A precision potentiometer was used to continuously measure the angular frequency of the follower link. A data acquisition system was configured to sample the follower orientation and the strains at each of the four locations. The sampling rate was set to 400 Hz; and a Butterworth filter was used with the pass band set to 150 Hz and the stop band set at 200 Hz. While the apparatus allows the mechanism to be operated over a range of speeds, the data presented herein corresponds to a near-sinusoidal crank excitation frequency of 0.92 Hz.

Dynamic beam deflection measurements were obtained with an *off-the-shelf* digital camera. After determining the dial zeros of the rocker extrema, still images can be mapped to potentiometer data recording the angular position of the rocker. Then using a novel technique to remove the projective linear distortion from the scene, scaled measurements can be made directly from the post-processed images. Beam tip and intermediate point lateral and longitudinal deflections were thus measured without contacting the oscillating beam. These deflections are then compared to the simulation predictions of lateral deflections.

2.1. Linkage input/output equations

The input/output equation for the four-bar linkage illustrated in Fig. 3 is obtained using elementary Cartesian analysis. The mechanism is a Grashof crank-rocker where the ith input crank angle is ψ_i, and the corresponding rocker output angle is φ_i. The link lengths are denoted a_i, $i \in \{1, 2, 3, 4\}$. To derive a useful form of the output angle φ in terms of the input angle ψ the position vectors for points P and Q located on the distal revolute pair centres in the crank and rocker, respectively, are used. The coupler, a_3, is modelled as a rigid body of fixed length. This length must be equal to the 2-norm of the vector difference $\{p\} - \{q\}$. The position vectors may be expressed as:

$$\{p\} = \left\{ \begin{array}{c} a_2 \cos \psi \\ a_2 \sin \psi \end{array} \right\}, \tag{1}$$

$$\{q\} = \left\{ \begin{array}{c} a_1 + a_4 \cos \varphi \\ a_4 \sin \varphi \end{array} \right\}. \tag{2}$$
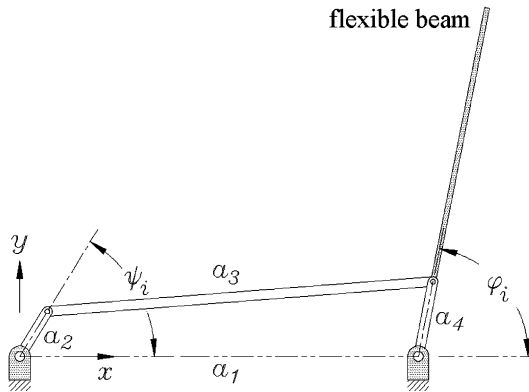
Fig. 3. The four-bar linkage used to generate the motion of the flexible beam.

Invoking the Pythagorean theorem, it must be that

$$a_3^2 = (x_p - x_q)^2 + (y_p - y_q)^2, \tag{3}$$

or, using Eqs. (1) and (2)

$$a_3^2 = (a_2 \cos \psi - a_1 - a_4 \cos \varphi)^2 + (a_2 \sin \psi - a_4 \sin \varphi)^2. \tag{4}$$

Eq. (4) can be expanded, and rewritten as [4,5]

$$A \sin \varphi + B \cos \varphi + C = 0, \tag{5}$$

where

$$A = \sin \psi,$$
$$B = \cos \psi - \frac{a_1}{a_2},$$
$$C = \frac{a_1 \cos \psi}{a_4} - \frac{a_1^2 + a_2^2 - a_3^2 + a_4^2}{2 a_2 a_4}.$$

A straightforward quadratic equation in the tangent of the half angle is obtained using the half-angle trigonometric substitutions

$$\sin \varphi = \frac{2 \tan(\varphi/2)}{1 + \tan^2(\varphi/2)}, \qquad \cos \varphi = \frac{1 - \tan^2(\varphi/2)}{1 + \tan^2(\varphi/2)}$$

in Eq. (5) yielding:

$$f(\varphi) = 2A \tan(\varphi/2) + B(1 - \tan^2(\varphi/2)) + C(1 + \tan^2(\varphi/2)) = 0. \tag{6}$$

Solving for $\tan \varphi/2$ leads to

$$\tan(\varphi/2) = \frac{A \pm \sqrt{A^2 + B^2 - C^2}}{B + C}. \tag{7}$$

For each distinct value of ψ the quantities A, B, and C, may be computed, and two distinct values of the output angle φ, corresponding to the *elbow-up* and *elbow-down* configurations, result:

$$\varphi = 2\arctan\frac{A \pm \sqrt{A^2 + B^2 - C^2}}{B + C}. \tag{8}$$

The *elbow-up* configuration is given by the positive radicand, giving the input/output angles for the linkage in Fig. 3.

2.2. Extrema

For the motion generating Grashof crank-rocker linkage the link lengths are:

$a_1 = 340$ mm,

$a_2 = 45$ mm,

$a_3 = 330$ mm,

$a_4 = 65$ mm.

Substituting these values into Eq. (8) yields the input/output equation

$$\varphi = 2\arctan\left(\frac{3}{5}\frac{\left[4\sin\psi + 2\sqrt{5056 - 2601\cos^2\psi} + 765\cos\psi\right]}{99\cos\psi + 125}\right). \tag{9}$$

The extreme output angles occur for values of the input angle, ψ that satisfy the first derivative of Eq. (6) with respect to the output angle, φ:

$$\frac{\mathrm{d}f(\varphi)}{\mathrm{d}\varphi} = -2\arctan\left(\frac{A}{-B+C}\right) = -2\arctan\left(\frac{117}{5}\frac{\sin\psi}{99\cos\psi + 125}\right) = 0. \tag{10}$$

Values of ψ that satisfy Eq. (10) are $n\pi$, where n is any integer. For $n =$ an even integer (including 0), the corresponding elbow-up output angle is $\varphi = 62.598°$. For $n =$ an odd integer, the corresponding elbow-up output angle is $\varphi = 150.474°$. The linkage in these two extreme configurations is illustrated in Fig. 4. The nominal rocker output angular range is

$$\Delta\varphi = 150.474° - 62.598° = 87.876°. \tag{11}$$
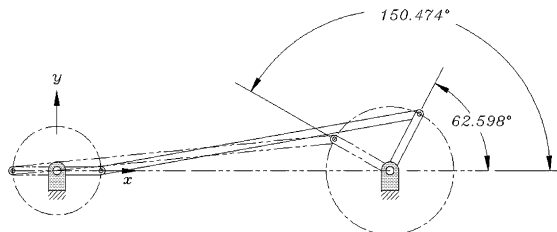

Fig. 4. Output extrema of the linkage.

3. Multibody dynamics formulation

This section provides an overview of the analytical flexible multibody dynamics formulation that has been developed and applied for automatically generating and solving the equations of motion of the reciprocating beam problem. The formulation does not place limiting restrictions on the flexible bodies in terms of the magnitude of deformation or the level of internal damping.

The first step in the automated analysis is to determine the system topology and assign configuration coordinates and generalized speeds to the system. The Hopcroft and Tarjan version of the depth first search algorithm [6] is used to identify a unique path from ground to each body in the system. Rigid body configuration coordinates accounting for joint motion $\{q_r\}$ and flexibility coordinates accounting for deformation of flexible bodies $\{q_f\}$ are assigned along the paths. The actual flexible bodies consist of flexible element bodies interconnected by fixed joints. The deformation field within flexible bodies is discretized using a finite element approach where each element is treated as a separate body. The deformation field in body i can be written

$$\{d_{ij}\} = [N_{ij}]\{q_{f_i}\}, \tag{12}$$

where $[N_{ij}]$ are the finite element shape functions for body i evaluated at location j.

The generalized speed vector $\{u\}$ is defined as the time derivative of the configuration coordinate vector

$$\{u\} = \{\dot{q}\}. \tag{13}$$

Using the configuration coordinates and generalized speeds, the position and velocity functions for the system are developed. These functions may be used to evaluate the position and velocity of all important points in the system.

Consider the body illustrated schematically in Fig. 5. The dashed line indicates the deformed shape of body i. The position $\vec{p}_{ij}$ of differential volume j on body i is expressed in global coordinates as

$$\vec{p}_{ij} = \vec{p}_{A_{i-1}} + \vec{p}_{A_i/A_{i-1}} + [T_i]\left(\vec{r}_{j/A_i} + \vec{d}_{ij}\right) \tag{14}$$

and the velocity $\vec{v}_{ij}$ is obtained directly by differentiating the position function (Eq. (14))

$$\vec{v}_{ij} = \dot{\vec{p}}_{A_{i-1}} + \dot{\vec{p}}_{A_i/A_{i-1}} + [T_i]\dot{\vec{d}}_{ij} + [\dot{T}_i]\left(\vec{r}_{j/A_i} + \vec{d}_{ij}\right), \tag{15}$$
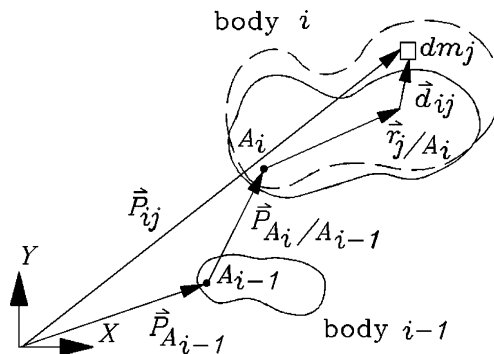

Fig. 5. Schematic representation of a single body.

where the vectors are defined in Fig. 5 and $[T_i]$ is the rotational transformation matrix from the local coordinates of body i to global coordinates.

Eq. (15) can be used to evaluate the instantaneous velocity of any point in the system as a linear function of the generalized speeds, allowing a composite velocity vector $\{V\}$ to be written

$$\{V\} = [V]\{u\}, \tag{16}$$

where $[V]$ is the partial velocity matrix which reflects how each generalized speed affects the velocity of each key point in the system.

Kane's equation without multipliers [7] is used to formulate the dynamic equations numerically at each time step. It states

$$\{Q^*\} + \{Q^e\} + \{Q^i\} = \{0\}, \tag{17}$$

where $\{Q^*\}$ is a vector of generalized inertia forces; $\{Q^e\}$ is a vector of generalized external forces; and $\{Q^i\}$ is a vector of generalized internal forces.

The contribution of each individual body to the generalized inertia force is obtained by differentiating the momentum function of the body. The resulting contribution is of the form

$$\{Q_i^*\} = \{Q_V^*\} + [Q_M^*]\{\dot{u}\}, \tag{18}$$

where $\{Q_V^*\}$ contains centripetal and Coriolis force terms that can be evaluated from known configuration coordinates and generalized speeds; the second term depends on unknown derivatives of generalized speeds.

The generalized external force vector $\{Q^e\}$, if applicable, is evaluated by considering the effect of each non-constraint applied force on each degree of freedom. This is accomplished by mapping forces onto the degrees of freedom using the partial velocity matrix $[V]$ such that

$$\{Q_k^e\} = [V_{ik}]^T\{F_k\}, \tag{19}$$

where $\{F_k\}$ represents force k acting on body i.

The generalized internal force contribution from each body results from strain-induced stiffness forces $\{Q_{is}^i\}$ and strain-rate-produced damping forces $\{Q_{id}^i\}$

$$\{Q_i^i\} = \{Q_{is}^i\} + \{Q_{id}^i\}. \tag{20}$$

Moderate to large deformation causes the nonlinearity between strain and displacement to become an important consideration in developing the element equations [8].

The approach that is used in this formulation involves describing the deformation field using a full set of orthogonal coordinates and forming the total strain energy as a function of the strain (or displacements) only. Strains are defined with the nonlinear strain displacement relations offering accuracy, generality, and widespread applicability.

The potential energy functional π_p for a single flexible element in a multibody system, such as the one shown in Fig. 6, is formed in the same way as is done in conventional finite element analysis [9,10]

$$\left\{\frac{\partial \pi_p}{\partial \Delta_r}\right\} = ([K_e] + [K_\sigma])\{\Delta_r\} - \{F_n\} = \{0\}, \tag{21}$$
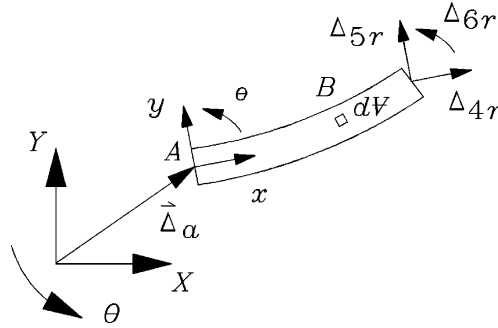
Fig. 6. Flexible planar beam element.

where $\{F_n\}$ is a vector of nodal reaction forces in local coordinates, $\{\Delta_r\}$ is a vector of element nodal displacements in element local coordinates, and the total element stiffness matrix $[K_T]$ comprises the elastic stiffness matrix $[K_e]$ and the geometric stiffness matrix $[K_\sigma]$.

The multibody dynamics formulation development requires an expression for $\{\partial\pi_p/\partial q\}$ which is the vector of partial derivatives of the potential energy functional for an element with respect to each of the generalized coordinates q_i in the multibody system. The chain rule allows this vector to be expanded

$$\left\{\frac{\partial\pi_p}{\partial q}\right\} = \left\{\frac{\partial\pi_p}{\partial\Delta_r}\right\}^T \left[\frac{\partial\Delta_r}{\partial q}\right]. \tag{22}$$

Next, the nodal displacements are linearized about the current configuration

$$\{\Delta_r\} = \{\Delta_{r0}\} + \{\delta\Delta_r\} \tag{23}$$

where $\{\Delta_{r0}\}$ is a vector of nominal nodal displacements and $\{\delta\Delta_r\}$ is a vector of small changes in relative nodal displacements. These changes can be linearly related to the generalized coordinates

$$\{\delta\Delta_r\} = [T]^T[A]\{\delta q\}, \tag{24}$$

where $[A]$ is the transformation matrix relating nodal displacements to multibody coordinates in the global coordinate system and $[T]$ is the coordinate transformation from element global to local coordinates. Differentiating Eq. (24) with respect to $\{q\}$ yields

$$\left[\frac{\partial\Delta_r}{\partial q}\right] = [T]^T[A]. \tag{25}$$

By comparing expressions for the absolute velocity of the element nodes, it can be shown that $[A]$ is a matrix analogous to $[V]$ but relating the nodal velocity components to the generalized speeds.

Substituting Eqs. (21) and (25) into Eq. (22) and transposing the result produces the column vector of generalized internal forces caused by internal stiffness

$$\{Q_{is}^i\} = \left\{\frac{\partial\pi_p}{\partial q}\right\}^T = [A_i]^T[T]([K_e] + [K_\sigma])\{\Delta_r\}. \tag{26}$$

This result can be added directly to the system generalized internal force vector (Eq. (20)).

The generalized internal forces generated by material damping within flexible elements are treated analogously. The contribution of nodal damping forces $\{F_{nd}\}$ to the generalized internal force vector is

$$\{Q_{id}^i\} = [A_i]^T [T] \{F_{nd}\}. \tag{27}$$

The expression for $\{Q_{id}^i\}$ remains general. Damping within flexible bodies can be included provided that $\{F_{nd}\}$ can be calculated from the state of the system and time. This provides maximum flexibility in the choice of damping model used for representing material damping within flexible bodies. For the simple case of proportional damping

$$\{F_{nd}\} = (a_0[M] + a_1[K_T])\{\dot{\Delta}_r\}, \tag{28}$$

where $[M]$ is the consistent element mass matrix [9,10] and $\{\dot{\Delta}_r\}$ is the vector of first time derivatives of the element relative nodal displacements.

For the six-degree-of-freedom planar beam element shown in Fig. 6, the deformation field within each element is expressed in terms of the nodal degrees-of-freedom using the shape functions

$$u(x) = \frac{x}{L}\Delta_4 \tag{29}$$

and

$$w(x) = \left(3\left(\frac{x}{L}\right)^2 - 2\left(\frac{x}{L}\right)^3\right)\Delta_5 + \left(\frac{x^2}{L}\left(\frac{x}{L} - 1\right)\right)\Delta_6, \tag{30}$$

where u corresponds to the local longitudinal direction of the beam element and w corresponds to the lateral direction.

The corresponding right halves of the stiffness matrices are

$$[K_e] = \begin{bmatrix} -\dfrac{EA}{L} & 0 & 0 \\[2mm] 0 & -\dfrac{12EI}{L^3} & \dfrac{6EI}{L^2} \\[2mm] 0 & -\dfrac{6EI}{L^2} & \dfrac{2EI}{L} \\[2mm] \dfrac{EA}{L} & 0 & 0 \\[2mm] 0 & \dfrac{12EI}{L^3} & -\dfrac{6EI}{L^2} \\[2mm] 0 & -\dfrac{6EI}{L^2} & \dfrac{4EI}{L} \end{bmatrix} \tag{31}$$

and

$$[K_\sigma] = P \begin{bmatrix} -\dfrac{3}{L} & 0 & 0 \\[2mm] 0 & -\dfrac{6}{5L} & \dfrac{1}{10} \\[2mm] 0 & -\dfrac{1}{10} & -\dfrac{L}{30} \\[2mm] \dfrac{3}{L} & 0 & 0 \\[2mm] 0 & \dfrac{6}{5L} & -\dfrac{1}{10} \\[2mm] 0 & -\dfrac{1}{10} & \dfrac{2L}{15} \end{bmatrix}, \tag{32}$$

where

$$P = \frac{EA}{L}\Delta_4. \tag{33}$$

Numerical solutions to the overall approach can be obtained by substituting Eq. (18) into Kane's equation (Eq. (17)) and rearranging the resulting governing equations so that the only dependence on the unknown derivatives of generalized speeds is on the left-hand side of the equation

$$[Q_M^*]\{\dot{u}\} = -(\{Q_V^*\} + \{Q^e\} + \{Q^i\}). \tag{34}$$

The dynamic solution then consists of:

1. building Eq. (34) numerically and solving it for the unknown derivatives of the generalized speeds, $\{\dot{u}\}$;
2. integrating $\{\dot{u}\}$ to obtain the generalized speeds, $\{u\}$, at the next time step; and
3. integrating the generalized speeds $\{u\}$ to obtain the configuration coordinates at the next time step.

This procedure is repeated for the duration of the simulation. Numerical integration has been performed using the IMSL DDRIV2 explicit multi-step integration routine developed by Kahaner and Sutherland [11]. The integrator continuously evaluates the numerical stiffness of the equations and for non-stiff equations uses a variable-order adaptive-time-step Adams method; for stiff equations, it switches to Gear's method. Absolute and relative integration tolerances were both set to 10^{-4}.

An expanded form of the formulation presented here, that includes capability for automatically analyzing systems containing closed kinematic loops has been implemented in the flexible multibody computer program FLXDYN that has been validated for open- and closed-loop systems that contain both rigid and flexible bodies [3].

The formulation is found to be efficient and versatile for predicting the forward dynamics of multibody systems, including systems containing heavily damped very flexible substructures.

For the specific case of the reciprocating flexible beam problem, the multibody system used for the analysis comprises two flexible beam elements. The inboard end of the inboard element is connected to ground by a revolute joint. The inboard end of the outboard element is effectively cantilevered to the outboard end of the inboard element using a 'fixed' joint. Seven generalized coordinates are required to describe the system kinematics: q_1 is the rotational degree-of-freedom through the revolute joint; q_2 through q_4 are the longitudinal deflection, lateral deflection, and rotation of the outboard end of the inboard element defined in a coordinate system rotating with the inboard end of the beam; q_5 through q_7 are similar coordinates for the outboard element and defined in a coordinate system attached to the inboard end of the outboard element. Experience with the experimental apparatus indicates that, for the external excitation frequencies considered, the dynamic response of the flexible beam is dominated by the first mode of beam vibration. Consequently, a two-flexible-element representation of the system is considered adequate.

The revolute joint angle and angular velocity are effectively prescribed functions of time with the four-bar mechanism generating the input forcing function. The prescribed motion is introduced into the multibody dynamic formulation by rearranging and partitioning Eq. (18) such that

$$
\begin{bmatrix} Q_{pp}^* & Q_{pu}^* \\ Q_{up}^* & Q_{uu}^* \end{bmatrix} \begin{Bmatrix} \dot{u}_p \\ \dot{u}_u \end{Bmatrix} = \begin{Bmatrix} G_p(q_p, q_u, u_p, u_u, t) \\ G_u(q_p, q_u, u_p, u_u, t) \end{Bmatrix},
\tag{35}
$$

where subscript p indicates prescribed values that are known functions of time and subscript u indicates unprescribed values, and $\{G\}$ has been used to represent the generalized right-hand side force vector for simplicity and clarity. The lower partition of Eq. (35) can be solved for the unknown derivatives of the unprescribed generalized speeds $\{\dot{u}_u\}$

$$
[Q_{uu}^*]\{\dot{u}_u\} = \{G_u(q_p, q_u, u_p, u_u, t)\} - [Q_{up}^*]\{\dot{u}_p\}.
\tag{36}
$$

Next, if desired, the upper partition of Eq. (36) can be solved for the prescribed forces required to produce the prescribed motion. In this particular application, the prescribed generalized coordinate and generalized speed is q_1 and u_1 respectively, with all others being unprescribed.

The effective system damping results both from internal material damping and aerodynamic damping. Using the experimental apparatus, it should be possible to obtain modal damping ratios corresponding to the first and second vibration modes. These damping ratios can in turn be related to the proportional damping coefficients used in the multibody dynamic formulation (refer to Eq. (28)) [12] such that

$$
\zeta_n = \frac{1}{2\omega_n} \sum_i a_i \omega_n^{2i},
\tag{37}
$$

where ω_n is the frequency of mode n. Letting i equal 0 and 1 for proportional damping

$$
\begin{Bmatrix} \zeta_1 \\ \zeta_2 \end{Bmatrix} = \begin{bmatrix} \dfrac{1}{2\omega_1} & \dfrac{\omega_1}{2} \\ \dfrac{1}{2\omega_2} & \dfrac{\omega_2}{2} \end{bmatrix} \begin{Bmatrix} a_0 \\ a_1 \end{Bmatrix}.
\tag{38}
$$

This equation is solved for the proportional damping coefficients by inverting the coefficient matrix resulting in

$$\begin{Bmatrix} a_0 \\ a_1 \end{Bmatrix} = \frac{2}{\omega_2^2 - \omega_1^2} \begin{bmatrix} \omega_1 \omega_2^2 & -\omega_1^2 \omega_2 \\ -\omega_1 & \omega_2 \end{bmatrix} \begin{Bmatrix} \zeta_1 \\ \zeta_2 \end{Bmatrix}. \tag{39}$$

Results obtained from using the dynamic formulation are compared with measured displacement results in Section 5.2.

4. Digital image processing

An *off-the-shelf* digital camera was used to acquire images: the Canon Powershot A70. The idea was to explore if obtaining high quality deflection measurements was feasible using a relatively low-cost camera. The camera has an array of approximately 3.2 million pixels, suggesting that employing centre-of-area computations could yield the coordinates of very accurate construction points to characterize the beam centre line.

After application of segmentation and filtering algorithms the spurious background data in the raw digital image is annihilated. The best-fit beam centre line is established using Prewitt edge detection and a two-dimensional moment computation about the vertical and horizontal pixel directions yielding a two-dimensional vector of construction points through the longitudinal beam centre line to sub-pixel accuracy. The following describes the techniques used.

4.1. Mean convolution mask

A convolution mask is an $m \times n$ dimensional window that is centred on each element in the image data matrix. One of the simplest such noise reduction masks to implement is the *mean filter*, or *mean convolution mask* [13]. The benefit of implementing this filter is that local peaks and valleys in pixel intensity caused by noise will be reduced. The value of each pixel intensity, $p(i, j)$, is replaced by the average of all the $m \times n$ values in the local neighbourhood:

$$p(i,j) = \frac{1}{M} \sum_{(m,n) \in N} f(m,n), \tag{40}$$

where M is the total number of pixels in the neighbourhood N. In this paper we use a 3×3 neighbourhood about (i, j) whose elements are all set equal to 1 giving

$$p(i,j) = \frac{1}{9} \sum_{m=(i-1)}^{i+1} \sum_{n=(j-1)}^{j+1} f(n,m). \tag{41}$$

The effects of applying this mean filter to the segmented scene is illustrated by Fig. 7(a) and (b).

4.2. Sub-pixel accuracy

The lateral deflection of selected points on the longitudinal centre line of the beam edge seen in Fig. 7(b) is estimated by first detecting the bounding edges with a Prewitt operator [14]. An edge
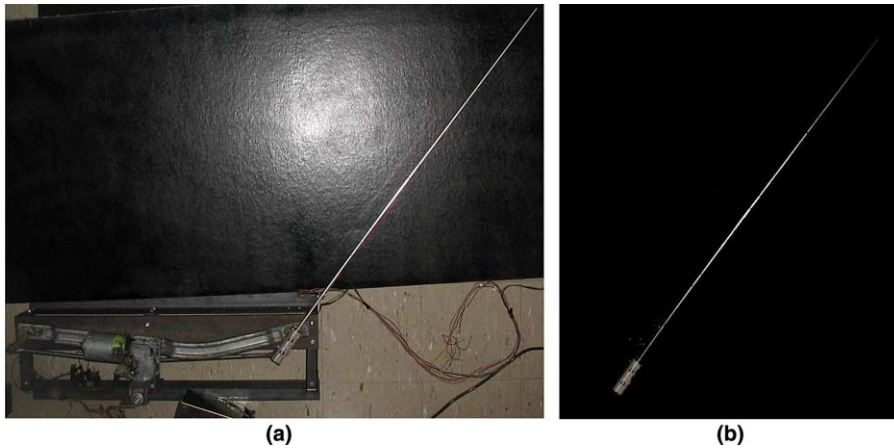
Fig. 7. (a) Raw digital image; (b) same image after filtering.

detection operator is another type of convolution mask whose elements are weighted such that the weighted sum of the elements in the product of the mask with image data produce larger intensities in the proximity of sharp transitions between adjacent pixels. The elements of these convolution masks can be weighted to accentuate pixels containing horizontal or vertical edges with transitions from high to low or low to high intensity (Fig. 8).

The hub angle is computed after establishing its best-fit centre line [15]. The angle of this centre line is then computed relative to the horizontal pixel direction. A 5×1 *boxcar operator* [14] is then used to smooth the detected edge pixels. The centre of area of the edge pixels is then computed by establishing their moment centres in two-dimensions [16]. The result is a set of construction points for the centre line of the beam edge given in sub-pixel accuracy coordinate pairs.
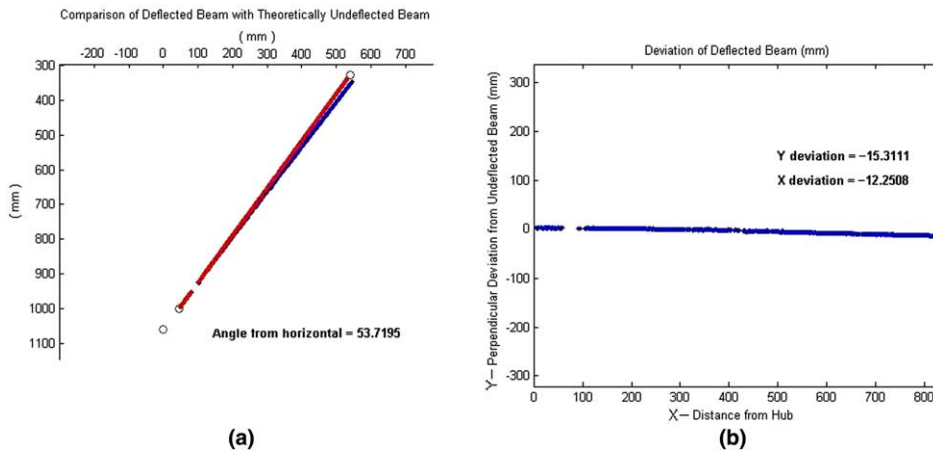

Fig. 8. (a) Deflected and undeflected reference beam; (b) hub angle and tip deflection computed to sub-pixel accuracy.

4.3. Projective distortion correction

Metric data in digital images acquired with a camera are necessarily subject to projective distortion destroying the Euclidean metric. An image of a registration object of known geometry can be used to eliminate this distortion and restore the Euclidean metric [17].

Two distinct sets of four points in the projective plane P_2 uniquely determine a projective collineation if the points in the two sets are distinct, and if no three points are on the same line. Let the first set of four points have the coordinates $W(W_0 : W_1 : W_2)$, $X(X_0 : X_1 : X_2)$, $Y(Y_0 : Y_1 : Y_2)$, and $Z(Z_0 : Z_1 : Z_2)$. Let the second set of four points have the coordinates $w(w_0 : w_1 : w_2)$, $x(x_0 : x_1 : x_2)$, $y(y_0 : y_1 : y_2)$, and $z(z_0 : z_1 : z_2)$.

When expressed as a vector, the ratios implied by the homogeneous coordinates can be scaled by an arbitrary factor:

$$\{w_0 : w_1 : w_2\}^{\mathrm{T}} = \mu\{w_0 : w_1 : w_2\}^{\mathrm{T}}. \tag{42}$$

The corresponding affine coordinates are

$$x_w = \frac{\mu w_1}{\mu w_0}, \qquad y_w = \frac{\mu w_2}{\mu w_0}. \tag{43}$$

This is why different scalar multiples of a set of homogeneous coordinates represent the same point in the projective plane.

The projective collineation may be viewed as a linear transformation that maps the coordinates of a point described in a particular coordinate system onto the coordinates of a different point in the same coordinate system. The geometry can be represented by the vector–algebraic relationship

$$\lambda \begin{Bmatrix} W_0 \\ W_1 \\ W_2 \end{Bmatrix} = \mu \begin{bmatrix} t_{11} & t_{12} & t_{13} \\ t_{21} & t_{22} & t_{23} \\ t_{31} & t_{32} & t_{33} \end{bmatrix} \begin{Bmatrix} w_0 \\ w_1 \\ w_2 \end{Bmatrix}. \tag{44}$$

Without loss in generality, we can set $\rho = \lambda/\mu$ and express Eq. (44) more compactly as

$$\rho\{W\} = [T]\{w\}. \tag{45}$$

The elements of the linear transformation matrix depend on the details of the mapping. As it represents a general projective collineation there are no orthogonality conditions on the rows or columns of $[T]$. This means that the elements can take on any numerical value. Thus the mapping between two points in an arbitrary collineation consists of nine variables. If we wish to determine the mapping given a point and its image then $[T]$ represents nine unknowns, but, because of the use of homogenous coordinates, at most eight are independent. Still, to remain general the scaling factor ρ must be counted among the unknowns because the given points come from a Cartesian coordinate system while the mapping is projective. The result is that the coordinates of four points, along with those of their images, are enough to uniquely define the eight independent elements of the transformation matrix and the four independent scaling factors, ρ_i, $i \in \{1, 2, 3, 4\}$.

The vertices of an arbitrary quadrilateral represent four points W, X, Y, and Z. We consider the image of these four points w, x, y, and z, to be the vertices of a quadrilateral whose dimensions are known, centred on the origin of the coordinate system in which the quadrilateral is defined. Now a

set of equations must be written so that the elements of $[T]$ can be computed in terms of the point and image coordinates:

$$t_{11}w_0 + t_{12}w_1 + t_{13}w_2 - \rho_1 W_0,$$
$$t_{21}w_0 + t_{22}w_1 + t_{23}w_2 - \rho_1 W_1,$$
$$t_{31}w_0 + t_{32}w_1 + t_{33}w_2 - \rho_1 W_2,$$
$$t_{11}x_0 + t_{12}x_1 + t_{13}x_2 - \rho_2 X_0,$$
$$\vdots$$
$$t_{31}z_0 + t_{32}z_1 + t_{33}z_2 - \rho_4 Z_2. \tag{46}$$

Eq. (46) represent 12 equations in 13 unknowns, however we can set $t_{11} = 1$. It is a simple matter to solve for the 12 unknowns, however we only require the eight elements of $[T]$.

In the experiment a registration object consisting of a pair of orthogonal grooves intersecting in a square of known geometry was used. It was placed in the scene containing the beam and photographed. The image of the four corners of the known quadrilateral were used to compute the $[T]$ used to *straighten* the lines in subsequent images and to provide a scaling factor. This action compensates only for linear projective and not higher order radial distortion. We assume the linear component is dominant and thereby forego the need for a full camera calibration.

5. Results and discussion

5.1. Static loading

A test was performed to verify the output of FLXDYN under static loading conditions. These results were compared to theoretical deflections based on beam geometry, properties, and tip load, as well as those based on measured surface strain. The beam was removed from the crank-rocker mechanism and set up such that it would bend in a vertical plane as the result of weights associated with masses of different magnitude suspended from its free end. The tip displacements and strains at locations of interest resulting from the tip loads were measured and predicted. Care was taken to exclude the influence of the self-weight of the beam from measurements and predictions.

5.1.1. Direct measurement
For each of the three masses used, repeated reading of a precision-ruled straight edge was used to directly measure the difference between the vertical position of the beam tip prior to application of the tip weights and the deflected positions once the weights were attached and the system was allowed to settle to equilibrium. These directly measured deflections are listed in Table 2.

5.1.2. Theoretical displacement
Knowing the material properties, geometry, and applied tip loads, a simple beam bending calculation was performed to ensure consistency between the beam parameters and the physical

Table 2
Strains (μ) and tip displacement (mm) associated with tip mass (kg)

	Strain 1	Strain 2	Strain 3	Strain 4	Tip displacement	Mass
Measured	191.00	143.00	96.00	52.00	26.99	0.051
Theoretical	186.63	141.34	96.05	50.53	26.84	
Estimate	190.69	143.35	96.76	50.71	27.23	
FLXDYN					27.91	
Measurement	361.00	272.00	185.00	100.00	51.59	0.100
Theoretical	362.64	274.64	186.63	98.18	52.14	
Estimate	360.35	273.04	185.76	98.08	51.86	
FLXDYN					53.84	
Measurement	534.00	403.00	276.00	148.00	78.18	0.149
Theoretical	537.82	407.30	276.78	145.60	77.33	
Estimate	533.01	404.90	276.14	146.08	76.90	
FLXDYN					79.38	

reality of the system. The beam tip deflection [18] was calculated for each of the three known tip weights using

$$\delta = \frac{1}{3} \frac{PL^3}{EI},\tag{47}$$

where E is Young's modulus for the beam material, I is the area moment of inertia of the beam, P is the magnitude of the applied force (weight), L is the distance between the force application point and the beam cantilever point, and δ is the deflection of the free end. The material parameter values used to represent the beam are provided in Table 3. The three theoretical tip deflection results are given in Table 2.

5.1.3. Bending theory estimate

Beam bending theory [18] relates beam surface strain, applied bending moment, and beam curvature such that

$$\frac{d^2 y}{dx^2} = \frac{\varepsilon}{h} = \frac{M}{EI},\tag{48}$$

where

$$M = (L - x)P\tag{49}$$

and y is the deflection of the beam along its length x from the clamped end, ε is strain, h is the distance from the centre line to the surface of the beam, and M is the bending moment present at position x along the beam.

Table 3
Flexible beam material parameters

Young's modulus, E	Density, ρ	Proportional damping coefficients, a_0, a_1
6.8900×10^{10} N/m^2	2.6882×10^3 kg/m^3	0.1 s^{-1}, 0.1 s

Consequently, using the known tip weights, it is possible to integrate the beam curvature calculated from Eq. (48) to predict the shape of the deflected beam and ultimately the tip deflection. While possible, this approach would not directly contribute to the required measurement approach as in the dynamic situation, the inertial loading along the length of the beam will not be known a priori. Consequently, instead, the measured strains at four locations were used to calculate the beam curvature. This data was then curve fitted along the length of the beam, and integrated, using appropriate boundary conditions, to obtain the beam deflected shape and tip deflection. Results are presented in Table 2. This approach is similar to [19].

5.1.4. Simulated results

The FLXDYN formulation described in Section 3 was also used to predict the beam tip deflection. Transient simulations were set up where the beam was allowed to settle to equilibrium under the influence of constant downward tip forces, corresponding to each of the three tip weights, from its initially undeflected condition. The results for the tip deflection are included in Table 2. Strains at each of the four strain gauge locations were not extracted from the FLXDYN simulation for the static case as strain evaluation is not a necessary intermediate step in the dynamic solution. Section 5.2 describes how strains can be evaluated through a post-processing step.

5.1.5. Static results

Inspection of the summary results presented in Table 2 shows excellent agreement between the measured, calculated, predicted, and simulated strains for the three static load cases considered. In general, the simulated results produced the largest tip deflections and those farthest from the directly measured values in two of three cases considered, though the difference was limited to 1.53–4.36% based on the measured values. This deviation is on the order of the resolution of the static deflection measurements themselves.

5.2. Dynamic results

5.2.1. Damping estimate

The geometric and material properties of the flexible beam were known or easily measured. This allowed inertial and stiffness properties of the beam to be determined directly. However, coefficients of the proportional damping model described in Section 3 had to be estimated experimentally. The preferred approach, also described in Section 3, is based on experimental determination of the damping ratios for the two lowest-frequency bending modes. Due to difficulties in exciting the second vibration mode in the experimental setup it was not possible to determine the proportional damping coefficients in this way. Instead, it was decided to assume equal coefficients a_0 and a_1 and to iteratively adjust their value until the logarithmic decrement for simulated strains at strain gauge location two agreed with those measured in an experiment where the beam tip was deflected, released from rest, and allowed to settle to its equilibrium position.

It should be noted that while strain is not a standard output from the FLXDYN simulation, it can readily be evaluated from the state variables. The FLXDYN formulation uses a complete expression for the axial fiber strain at a distance z above the centroidal axis of the beam such that

$$\epsilon_x = \frac{\partial u}{\partial x} + \frac{1}{2}\left(\frac{\partial u}{\partial x}\right)^2 + \frac{1}{2}\left(\frac{\partial w}{\partial x}\right)^2 - z\frac{\partial^2 w}{\partial x^2} - z\frac{\partial u}{\partial x}\frac{\partial^2 w}{\partial x^2} + \frac{1}{2}\left(z\frac{\partial^2 w}{\partial x^2}\right)^2, \tag{50}$$

where u and w are the deformation components in the axial and lateral directions at differential volume locations within the beam. The physical interpretation of each strain term follows.

- $\frac{\partial u}{\partial x}$ is the linear strain term that results from elongation of the beam.
- $\frac{1}{2}\left(\frac{\partial u}{\partial x}\right)^2$ is the nonlinear strain term resulting from elongation of the beam.
- $\frac{1}{2}\left(\frac{\partial w}{\partial x}\right)^2$ is the nonlinear strain term accounting for membrane strain caused by bending. The expression comes from a geometric interpretation of what happens to a segment length when bending occurs [9]. An approximation is made that is valid when $\left(\frac{\partial w}{\partial x}\right)^2 \ll 1$ which restricts the development to small relative rotations. In practice, beams may be modelled with a sufficient number of elements such that each one undergoes small rotations.
- $z\frac{\partial^2 w}{\partial x^2}$ is the contribution of bending to the axial strain for differential elements located a distance z away from the centroidal axis [9].
- $z\frac{\partial u}{\partial x}\frac{\partial^2 w}{\partial x^2}$ is a nonlinear coupling term between axial and bending effects at locations offset from the centroidal axis.
- $\frac{1}{2}\left(z\frac{\partial^2 w}{\partial x^2}\right)^2$ is the nonlinear term corresponding to bending.

However, for the small tip deflections occurring in this experiment, it is sufficient to consider only the linear strain contributions $\frac{\partial u}{\partial x}$ and $-z\frac{\partial^2 w}{\partial x^2}$.

The deformation field within the element is expressed in terms of the nodal degrees-of-freedom using the shape functions given in Eqs. (29) and (30). Differentiating these expressions with respect to x yields

$$\frac{\mathrm{d}u}{\mathrm{d}x}(x) = \frac{1}{L}q_x, \tag{51}$$

$$\frac{\mathrm{d}^2 w}{\mathrm{d}x^2}(x) = \left(\frac{6}{L^2} - \frac{12x}{L^3}\right)q_y + \left(\frac{6x}{L^2} - \frac{2}{L}\right)q_\theta, \tag{52}$$

where q_x, q_y, and q_θ are the generalized coordinates corresponding to beam element tip elongation, lateral deflection, and rotation; and x is the location of interest expressed relative to the inboard end of the beam element.

Using this approach resulted in proportional damping coefficients $a_0 = a_1 = 0.00087$. This value was then used in the reciprocating dynamic case. It was observed that this value grossly underestimated damping as evidenced by the amplitudes of the measured strains and the measured tip deflections. The need for higher damping is attributed to both higher rates of internal losses and aerodynamic damping in the relatively high-speed reciprocating beam case. Fig. 9 shows measured strains at each of the four strain gauge locations. Strains at each location are scaled versions of each other supporting the observation that the beam exhibits almost exclusively first-mode behaviour. Considering the strains at location two, the proportional damping coefficients were again adjusted until the mean strain amplitude trace shown for location two in Fig. 9 was
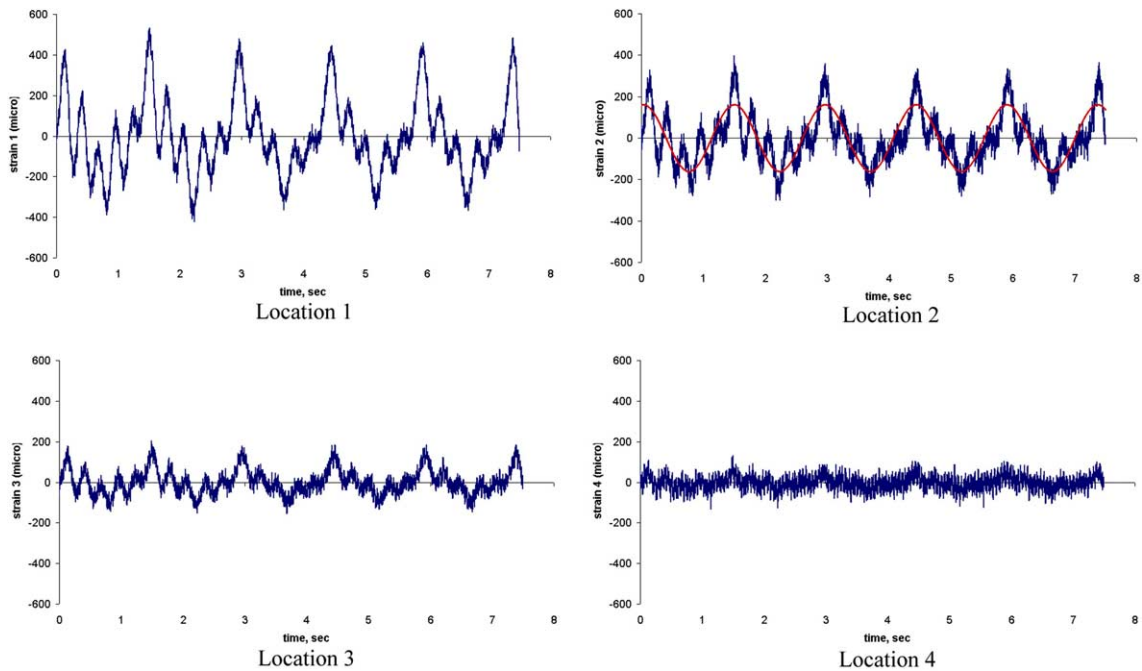
Fig. 9. Experimentally measured beam strain at locations 1, 2, 3, and 4; and simulated strain at location 2 (shown as the smooth line on the location 2 plot).

obtained. Proportional damping values $a_0 = a_1 = 0.1$ were found to much more closely reflect the experimental conditions. A more rigorous treatment of damping should be considered in future work.

5.2.2. Tip deflection

The input excitation function

$$\Phi = 0.7669 \sin(4.970t) \tag{53}$$

was used to prescribe the angle Φ of the inboard end of the beam as a function of time t. The angular velocity and angular accelerations of the inboard end of the beam result from successive time derivatives of Eq. (53).

Beam tip position versus time and input angle versus time results were output by the FLXDYN simulation described in Section 3.

Fig. 10 compares the simulated beam tip positions with the corresponding tip positions expected for a rigid beam. The graph shows the expected result that flexibility results in a greater range of y positions as the beam tip deflects beyond the range of motion of the rigid beam and that, as a result of deflection, the x tip position is often inboard of the corresponding rigid beam tip position.

The position results were then post-processed to extract the longitudinal (along the undeflected axis of the beam) and lateral (perpendicular to the undeflected axis of the beam) deflections relative to the hypothetical rigid beam. The steady-state results for lateral beam tip deflection versus
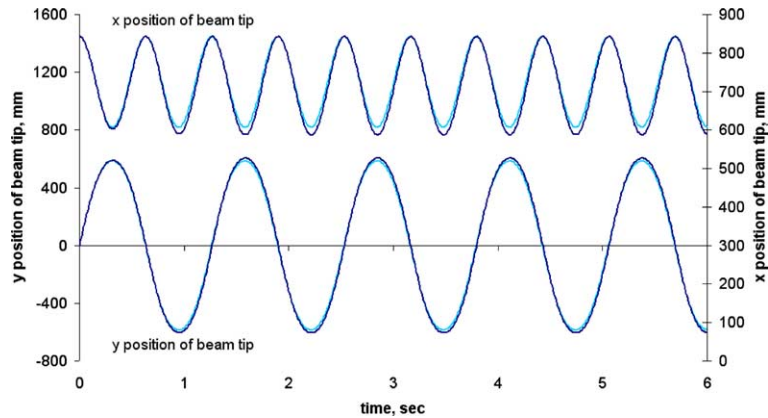
Fig. 10. Simulated flexible beam tip positions (dark) and corresponding rigid body beam tip positions (light).
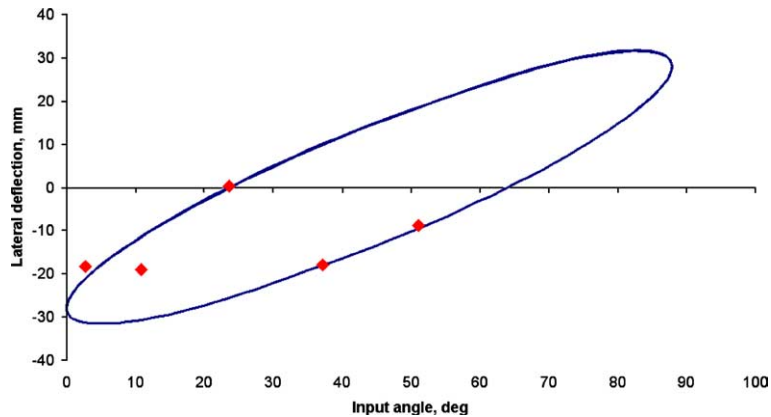

Fig. 11. Simulated (solid) and measured (points) lateral beam tip deflection versus input angle.

input angle are presented in Fig. 11. The plot was generated from three cycles of steady-state deflection data. The fact that a single contour exists confirms that steady state was indeed reached. The presence of two tip deflections for all input angles other than the input angle extrema reflects that tip deflections in opposite directions occur for opposite directions of travel of the beam during its reciprocating motion.

Tip deflection measurements during steady-state beam motion were made using the image processing outlined in Section 4. The contactless measurement system yielded large errors, but for an excitation period of approximately 0.92 Hz the system behaved reliably. This should not be taken as a condemnation of the approach, rather an indication that further work needs be done to improve its reliability.

Five hub angle and tip deflection pairs, such as those shown in Fig. 8(a) and (b) were obtained at 0.92 Hz excitation. These data points are plotted in Fig. 11, along with the simulated steady-state tip deflection versus input hub angle. While there are clearly insufficient tip deflection measurements to draw conclusions with statistically quantified certainty, general agreement between

simulated and available measured results is apparent. We believe this result to justify further investigation. To improve the measurement precision the camera radial distortion must be dealt with.

6. Conclusion

This paper introduced the reciprocating flexible beam problem as an interesting benchmark problem in flexible multibody dynamics. The system was described in sufficient detail to allow it to be modelled by other researchers. The FLXDYN multibody dynamics formulation was described and shown to be one valid method for predicting the flexible beam dynamic response. A novel image collection and processing approach using *off-the-shelf* components was described as an economical and effective method for non-contact tip deflection measurement. Using this approach, experimentally-measured tip deflections were shown to generally agree with simulated results. While a limited volume of data was collected in this study and rigorous statistical analysis was not possible, the results are encouraging and motivate further quantification of the experimental apparatus and refinement of the non-contact digital image processing measurement technique. Subsequent research must address limiting or modelling the effect of aerodynamic damping, increasing the amplitude of beam bending to span the range from geometrically linear to geometrically nonlinear deflection, and improving the image collection and processing technique to allow the collection of continuous deflection traces with higher resolution.

References

[1] W.J. Haering, R.R. Ryan, R.A. Scott, New formulation for flexible beams undergoing large overall plane motion, Journal of Guidance, Control, and Dynamics 17 (1) (1994) 76–83.
[2] J.P. Meijaard. Validation of flexible beam elements in dynamics programs, in: Manuel S. Pereira, Jorge A.C. Ambrósio, (Eds.), Computer Aided Analysis of Rigid and Flexible Mechanical Systems—vol. II Contributed Papers, pp. 229–245, Tróia, Portugal, June–July 1993, NATO—Advanced Study Institute.
[3] R.G. Langlois, R.J. Anderson, Multibody dynamics of very flexible damped systems, Multibody System Dynamics 3 (2) (1999) 109–136.
[4] R.S. Hartenberg, J. Denavit, Kinematic Synthesis of Linkages, McGraw-Hill, Book Co., New York, NY, USA, 1964.
[5] K.H. Hunt, Kinematic Geometry of Mechanisms, Clarendon Press, Oxford, England, 1978.
[6] S. Even, Graph algorithms. Computer Software Engineering Series, Computer Science Press, Rockville, Maryland, 1979.
[7] T.R. Kane, Dynamics of nonholonomic systems, Transactions of the ASME 28 (3) (1961) 574–578.
[8] I. Sharf, Geometric stiffening in multibody dynamics formulations, in: M. Wette, G.K. Man, (Eds.), Proceedings of the Fifth NASA/NSF/DOD Workshop on Aerospace Computational Control, Pasadena, California, February 1993. National Aeronautics and Space Administration, Jet Propulsion Laboratory, pp. 1–24.
[9] R.D. Cook, Concepts and Applications of Finite Element Analysis, second ed., John Wiley & Sons, New York, 1981.
[10] K.J. Bathe, Finite Element Procedures in Engineering Analysis, Prentice Hall, Inc., Englewood Cliffs, New Jersey, 1982.
[11] D. Kahaner, C. Moler, S. Nash, Numerical Methods and Software, Prentice Hall, Englewood Cliffs, NJ, USA, 1989.
[12] M. Paz, Structural Dynamics Theory and Computation, Van Nostrand Reinhold, Inc., New York, 1991.

[13] R. Jain, R. Kasturi, B.G. Schunck, Machine Vision, McGraw-Hill, New York, NY, USA, 1995.

[14] W.K. Pratt, Digital Image Processing, third ed., John Wiley and Sons, New York, NY, USA, 2001.

[15] A. Fratpietro, M.J.D. Hayes, Angle extraction using digital image processing, in: Proceedings of 19th Canadian Congress of Applied Mechanics (CANCAM), Calgary, AB, Canada, June 1–5, 2003, pp. 108–109.

[16] R. Ofner, P. O'Leary, M. Leitner, A collection of algorithms for the determination of construction points in the measurement of 3D geometries via light-sectioning, in: Wesic '99, 2nd Workshop on European Scientific and Industrial Collaboration promoting: Advanced Technologies in Manufacturing, Newport, South Wales, United Kingdom, 1999.

[17] M.J.D. Hayes, P.J. Zsombor-Murray, A. Gfrerrer, Largest ellipse inscribing an arbitrary polygon, in: Proceedings of the 19th Canadian Congress of Applied Mechanics (CANCAM 2003), University of Calgary, Calgary, AB, Canada, June 1–5, 2003, pp. 164–165.

[18] A. Higdon, E.H. Ohlsen, Mechanics of Materials, fourth ed., John Wiley and Sons, New York, NY, USA, 1985.

[19] S.J. Miller, J.C. Piedboeuf, Estimation of endpoint position and orientation of a flexible link using strain gauges, in: Proceedings of the Knowledge Based Systems and Robotics Workshop, 1993.